

PAPER

Cite this: *J. Mater. Chem. A*, 2018, 6, 7871**Bridge-type interface optimization on a dual-semiconductor heterostructure toward high performance overall water splitting†**Chong Wang,^a Bin Ma,^b Xingzhong Cao,^c Shan He,^a Jingbin Han,^{*a} Min Wei,^{*a} David G. Evans^a and Xue Duan^a

Interfacial carrier transportation is a key step in photocatalytic water splitting reaction. Herein, we fabricated a series of Cu₂O@ZnCr-layered double hydroxide (LDH) photocatalysts with tunable interfacial properties, by precise regulation over a covalent-bonding-bridge structure at the heterointerface. The Cu₂O@ZnCr-LDH photocatalyst with an optimized interface exhibits a stoichiometric production of H₂ and O₂ with a generation rate of 3.42 and 1.63 μmol h⁻¹, respectively, without any sacrificial agents or co-catalysts. This activity is among the highest reported for photocatalysts under the same conditions. By using extended X-ray absorption fine structure (EXAFS) and coincidence Doppler broadening positron annihilation spectroscopy (CDB-PAS), for the first time, we substantiated that a bridge-type bonding at the heterointerface strongly facilitates the interfacial transportation of photo-induced carriers via a Z-scheme route. This provides direct experimental evidence for carrier interfacial transportation, beyond previously reported theoretical predictions and simulations. It is expected that this modulation and optimization over the heterostructure interface can be extended to other dual-semiconductor photocatalysts with high performance.

Received 2nd March 2018
Accepted 29th March 2018

DOI: 10.1039/c8ta02001a

rsc.li/materials-a

Introduction

Semiconductor photocatalysts have evoked considerable attention in the fields of photovoltaic cells,^{1,2} water splitting^{3–5} and pollutant degradation.⁶ A photocatalyst with a single component generally suffers from inferior catalytic activity or poor photo-stability, which would be improved by constructing various heterojunction semiconductor photocatalysts, for instance, with a p–n junction^{7,8} and Z-scheme structure.^{9,10} The separation and directed migration of photo-induced carriers are two critical steps that play an important role in determining the efficiency of photocatalysts.¹¹ In some elaborately designed heterojunction photocatalysts, the separation of photo-induced hole–electron pairs has been achieved efficiently.^{12–14} However, for the following carrier transportation process through the

heterointerface, how to enable a directed and effective charge transfer instead of random flow still remains a challenging goal.

During the charge transfer process, the interface resistance of the heterojunction plays an important role in determining the efficiency of photo-induced carrier migration.¹⁵ In order to reduce the interface resistance, constructing a bridge structure to make two individual semiconductors more holistic at atomic and electronic levels provides a feasible route to achieve interface optimization.¹⁶ Actually, the existence of a bridge mediator for specific carrier-transfer has been proved in some phenylene oligomers¹⁷ and proteins systems,¹⁸ through the conjugated π, covalent or hydrogen bond to achieve a highly integrated donor–bridge–acceptor structure. Especially, our previous work reported the synthesis of a Cu₂O@ZnCr-layered double hydroxide (LDH) photocatalyst for visible-light-driven water splitting, in which the importance of interface interactions has been recognized.¹⁹ However, the carrier transfer mechanism at the heterointerface was still ambiguous, and a precise control over carrier transportation was not realized due to the difficulty of interfacial modulation.

In this work, we further improve the carrier transportation via precise regulation over the covalent-bonding-bridge structure at the heterointerface of Cu₂O@ZnCr-LDH, giving rise to a 4-fold enhancement in the water splitting rate compared with our previous work. The Cu₂O@ZnCr-LDH photocatalyst with an optimized bridge structure shows an extremely high gas-generation-rate of 3.42 and 1.63 μmol h⁻¹ for H₂ and O₂,

^aState Key Laboratory of Chemical Resource Engineering, Beijing Advanced Innovation Center for Soft Matter Science and Engineering, Beijing University of Chemical Technology, Beijing 100029, P. R. China. E-mail: hanjb@mail.buct.edu.cn; weimin@mail.buct.edu.cn

^bUniversité Grenoble Alpes, ISTERre, F-38000 Grenoble, France

^cInstitute of High Energy Physics, Chinese Academy of Sciences, Beijing 100049, P. R. China

† Electronic supplementary information (ESI) available: Details of characterization, SEM images, ICP-AES data, XRD, diffuse reflectance spectra, local structure obtained from EXAFS, current–potential curves, photoluminescence spectra and Nyquist plots. See DOI: 10.1039/c8ta02001a

respectively under visible light in the absence of sacrificial agents and co-catalysts. Based on extended X-ray absorption fine structure (EXAFS) and coincidence Doppler broadening positron annihilation spectroscopy (CDB-PAS) techniques, a direct and in-depth relationship between the modified interface and photocatalytic performance was revealed experimentally, beyond previously documented theoretical predictions and simulations.

Experimental

Synthesis of Cu₂O nanocubes

Cu₂O nanocubes were synthesized using a method similar to that reported in a previous study.¹⁹ Briefly, CuCl₂·2H₂O (1 mmol) was dissolved in deionized water (100 ml) with vigorous stirring, followed by drop-by-drop addition of a NaOH solution (2 mol L⁻¹, 10 ml). The mixed solution was maintained at 55 °C for 30 min. Subsequently, 20 ml of ascorbic acid (aq., 0.6 mol L⁻¹) was added dropwise into the dark brown solution. After aging for 3 h, a brick-red precipitate was obtained.

Synthesis of Cu₂O@ZnCr-LDH core-shell nanospheres

The Cu₂O@ZnCr-LDH core-shell nanospheres were prepared by using Cu₂O nanocubes as a soft template based on Pearson's hard and soft acid-base (HSAB) principle,²⁰ according to our previous work.¹⁹ 100 mg of freshly prepared Cu₂O was dispersed in deionized water (100 ml); then ZnCl₂ (50 mg, ~0.4 mmol) and CrCl₃·6H₂O (50 mg, ~0.2 mmol) were dissolved in this solution with magnetic stirring. Afterwards, a Na₂S₂O₃ solution (1 mol L⁻¹, 20 ml) was dropped into the above solution with stirring at room temperature for a fixed period (1–4 h). Finally, the resulting Cu₂O@ZnCr-LDH core-shell nanospheres were washed thoroughly with water and anhydrous ethanol, and then dried under freeze-drying for 12 h.

Measurements of the photocatalytic properties

The photocatalytic reaction was performed in a Pyrex glass cell with a constant temperature of 20 °C. The photocatalyst (20 mg) was suspended in ultrapure water (20 ml) and then thoroughly degassed with N₂. The photocatalytic performance toward water splitting was evaluated by monitoring the time dependent production of H₂ and O₂ under a CEL-HXUV300 Xe lamp (CEAULIGHT, China) with a filter ($\lambda > 420$ nm). The power intensity was fixed at 100 mW cm⁻² by controlling the distance between the photocatalytic reactor and the light source. All the tests were carried out without any sacrificial agents or co-catalysts. The amount of gas production was measured by using a gas chromatograph (GC-7890II; Techcomp. Co., Ltd.).

Characterization

Cu K-edge X-ray absorption spectroscopy (XAS) measurements were performed at beamline 1W1B of the Beijing Synchrotron Radiation Facility (BSRF) using a Si (111) double-crystal monochromator in the following two ways: routine test and excited state test. Briefly, the routine test was performed as usual to obtain the local coordination environment; the excited state test

data were collected under light irradiation to capture minor changes in the valence state resulting from the transient enrichment of carriers. The typical energy of the storage ring was 2.5 GeV with a maximum current of 250 mA. The Demeter software package was used for data integration and reduction of the X-ray absorption near edge structure (XANES) (Athena), as well as data fitting of the extended X-ray absorption fine structure (EXAFS) (Artemis). The pseudo radial distribution functions were obtained by Fourier transformation (FT) of the identical selected k^3 -weighted EXAFS oscillations using a Kaiser-Bessel window. Data fits were performed in inverse Fourier transform (FT⁻¹) using theoretical scattering paths calculated with FEFF8.4. For the excited XAS measurements, we used the same light source as in the photocatalytic reaction. Positron annihilation measurements were performed on a fast-slow coincidence ORTEC system with a time resolution of 187 ps for the full width at half-maximum. A 5×10^5 Bq source of ²²Na was sandwiched between two identical samples. The same Xe lamp with a filter ($\lambda > 420$ nm) was used for the measurements under light irradiation. The details of other characterization procedures are provided in the ESI.†

Results and discussion

By using Cu₂O nanocubes (size: ~200 nm, Fig. S1, ESI†) as the soft template, hollow Cu₂O@ZnCr-LDH nanospheres with a thin-layer Cu₂O core and LDH nanoplate shell were obtained. The formation mechanism of Cu₂O@ZnCr-LDH could be explained by the HSAB principle²⁰ and Kirkendall effect *via* the coordination effect between Cu⁺ and S₂O₃²⁻ ions. Firstly, the dissolved Cu⁺ ion as a soft acid reacts with the soft base S₂O₃²⁻, forming soluble [Cu₂(S₂O₃²⁻)_n]²⁻²ⁿ and OH⁻. Subsequently, a co-precipitation reaction of Zn²⁺ and Cr³⁺ occurs under this alkaline condition to produce ZnCr-LDH nanoplatelets on the surface of cubic Cu₂O, accompanied by the inward etching of Cu₂O caused by the Kirkendall effect. During the crystal growth of ZnCr-LDH nanoplatelets, the S₂O₃²⁻ anions enter into their gallery region to maintain the charge balance. This whole process results in the formation of hollow Cu₂O@ZnCr-LDH nanospheres with a thin-layer Cu₂O core and S₂O₃²⁻ intercalated ZnCr-LDH shell.

It has been observed in our previous work that the thickness of the Cu₂O layer could be adjusted by changing the synthesis duration from 10 min to 60 min, which resulted in a tunable water splitting performance.¹⁹ In this work, the reaction time was further prolonged from 1 h to 4 h to obtain a series of Cu₂O@ZnCr-LDH photocatalysts (denoted as S₁, S₂, S₃ and S₄, respectively). The elemental analysis result shows that the content of Cu remained almost at a constant level at ~6% (wt%, Fig. S2, ESI†). The scanning electron microscope (SEM) and transmission electron microscope (TEM) images (Fig. 1a and S3 and S4, ESI†) show that the ZnCr-LDH nanoplatelets (height: ~200 nm) are vertically aligned at the surface of the cubic-shaped Cu₂O core (size: ~200 nm, thickness: less than 5 nm). The crystal phase of the Cu₂O@ZnCr-LDH samples was further confirmed by XRD (Fig. 1b and S5†), which showed an interlayer spacing (d_{003}) of ~0.879 nm, corresponding to S₂O₃²⁻ ion

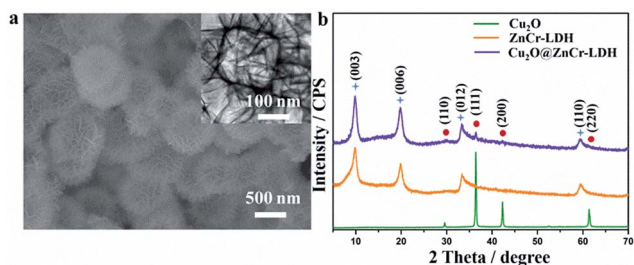


Fig. 1 (a) SEM and TEM (inset) images of the $\text{Cu}_2\text{O}@ZnCr\text{-LDH-S}_4$ sample, and (b) XRD patterns of Cu_2O , ZnCr-LDH and $\text{Cu}_2\text{O}@ZnCr\text{-LDH-S}_4$, respectively.

intercalated ZnCr-LDH . Diffuse reflectance spectra (Fig. S6, ESI[†]) confirm that the $\text{Cu}_2\text{O}@ZnCr\text{-LDH}$ samples are all visible-light-responsive. The results above indicate no obvious difference in the morphology, composition, crystal structure and light-response characteristics of $\text{S}_1\text{-S}_4$ samples. In spite of these similarities, the variation in photocatalytic performance among these samples is very large (Fig. 2a).

The H_2 and O_2 production rate increases gradually from S_1 to S_4 ; and the S_4 sample exhibits the largest H_2 and O_2 production rate of 3.42 and 1.63 $\mu\text{mol h}^{-1}$, respectively under visible light without any sacrificial agents or co-catalysts. This is 3.8 times higher than that of the S_1 sample, and superior to that of most reported overall water splitting photocatalysts under the same conditions.^{10,21,22} The apparent quantum efficiency (AQE) of all the samples was calculated according to the H_2 generation rate (Table S1, ESI[†]), which displays a regular enhancement from 0.20 to 0.76 for $\text{S}_1\text{-S}_4$ samples. The H_2 and O_2 production reaction was allowed to proceed for a total period of 25 h (with intermittent degassing every 5 h) without noticeable activity deterioration (Fig. 2b) and morphology change of the photocatalyst (Fig. S7, ESI[†]), indicating a high stability of $\text{Cu}_2\text{O}@ZnCr\text{-LDH}$ against photocorrosion. The significant difference in photocatalytic activity among the $\text{S}_1\text{-S}_4$ samples motivates us to probe the underlying reasons. We speculate that there might be some differences in their interfacial characteristics, which is probably relevant with the enhancement of photocatalytic activity.

X-ray absorption spectroscopy (XAS) was adopted to investigate the electronic structure and local coordination environment of the $\text{Cu}_2\text{O}@ZnCr\text{-LDH}$ photocatalysts. The normalized Cu K-edge XANES spectra of $\text{S}_1\text{-S}_4$ samples are shown in Fig. 3a,

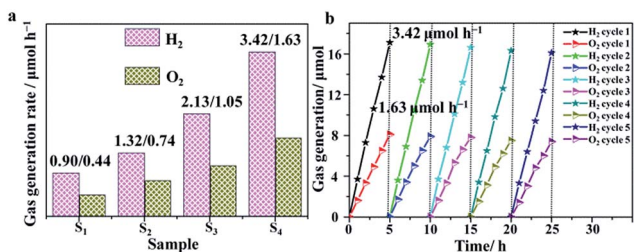


Fig. 2 (a) Gas generation rate of $\text{S}_1\text{-S}_4$ samples, and (b) gas generation as a function of irradiation time ($\lambda > 420\text{ nm}$) in 5 consecutive cycles (5 h per cycle) over the $\text{Cu}_2\text{O}@ZnCr\text{-LDH-S}_4$ photocatalyst.

with Cu foil, Cu_2O and CuO as the reference samples. The pre-edge peak position of the $\text{Cu}_2\text{O}@ZnCr\text{-LDH}$ samples is located at a photon energy range between the Cu_2O and the CuO reference, indicating that the valence of Cu in all samples is between +1 and +2, rather close to +1. Furthermore, the shape of the pre-edge peak and edge peaks for $\text{S}_1\text{-S}_4$ samples changes regularly (as shown in the arrow area and inset of Fig. 3a), providing compelling evidence for the change of the coordination environment around the Cu center atom. The k^3 -weighted EXAFS oscillations (Fig. 3b) are Fourier transformed into radial distribution functions (Fig. 3c and d), whose first neighbor shells are fitted with Cu-O and Cu-S backscattering pairs at $R = 1.95\text{ \AA}$ and 2.22 \AA , respectively. Compared with the first shell in the R space for Cu_2O at $R + \Delta R = 1.5\text{ \AA}$, all of these four $\text{Cu}_2\text{O}@ZnCr\text{-LDH}$ samples undergo a positive shift. This phenomenon is due to the replacement of Cu-O by the Cu-S bond *via* the formation of a $\text{Cu-(S}_2\text{O}_3^{2-})/\text{LDH}$ bridge structure at the heterointerface, which leads to a longer radial distance for the Cu center atom in $\text{Cu}_2\text{O}@ZnCr\text{-LDH}$ samples compared with that of Cu_2O . According to the EXAFS fitting results (Table S2, ESI[†]), we find that, for the samples from S_1 to S_4 , the coordination number (CN) of Cu-O decreases from ~ 1.34 to ~ 0.52 , and that of Cu-S increases from ~ 1.63 to ~ 2.68 , indicating the accumulation of Cu-S bonds at the heterointerface, with increasing the reaction time from 1 to 4 h.

To quantitatively describe the degree of interfacial modification by Cu-S bonding, we define an r -parameter based on the ratio of the coordination number of Cu-S and Cu-O bonds, as shown in eqn (1).

$$r = \frac{\text{CN}(\text{Cu-S})}{\text{CN}(\text{Cu-O})} \quad (1)$$

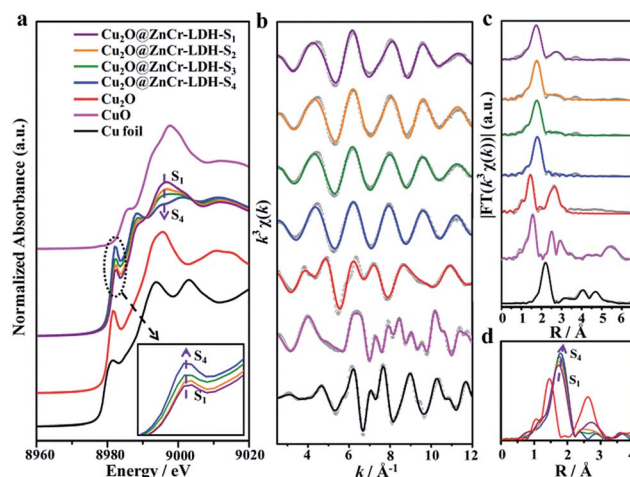


Fig. 3 (a) Normalized XANES signals with the enlarged pre-edge region (inset); (b) k^3 -weighted EXAFS oscillations; (c) Fourier transformed (not corrected for phase shift) EXAFS signals; the solid lines in b and c are the fitting results and the grey dots represent the experimental data; (d) overlaying of radial distribution functions for the $\text{S}_1\text{-S}_4$ samples and Cu_2O reference (all the curves are taken from c in order to provide a comparison). All the colorful curves are present in the same order in a, b and c.

With this description, the r -parameter was calculated as 1.22, 2.33, 3.73 and 5.15 for S_1 – S_4 samples, respectively. In addition, the $R + \Delta R$ value of the first neighbor shell becomes larger with the increased r -parameter (Fig. 3d), indicating a gradually enhanced average-bond-length of the first shell, caused by an improved extent of interfacial modification. For the signals of the higher shell at $R = 3.08 \text{ \AA}$, attributed to the Cu–Cu back-scattering pair, the intensity decreases with the increase of r -parameter. Especially for the S_4 sample with the highest r -parameter, the coordinate number of Cu–Cu almost decreases to zero (Fig. 3b and Table S2, ESI[†]), indicating an ultrathin disordered structure of the Cu_2O shell in the heterostructure.

In order to figure out the flow direction of the photo-generated electrons in the $\text{Cu}_2\text{O}@/\text{ZnCr-LDH}$ photocatalysts, excited state XAS was performed under light irradiation (Fig. 4a, $\lambda > 420 \text{ nm}$). The pre-edge absorption peak of the $\text{Cu}_2\text{O}@/\text{ZnCr-LDH}$ photocatalysts appears at 8982.65 eV without light irradiation; while it moves to 8982.32 eV (with a negative shift of 0.33 eV) upon illumination, which reveals an obvious transient decrease in the charge density of copper. In addition, the photon energy shift is accompanied by reversible on/off of the irradiation for several cycles (Fig. 4b). However, the radial distribution function in the Fourier transform (FT) of the EXAFS oscillations (Fig. 4c) does not undergo any shift when the light is switched on and off, indicating that the local coordination environment and the chemical bonds remain in the same state. The shift in the pre-edge is attributed to the transient change of the electronic structure arising from the photo-excited enrichment of electrons other than atomic structure change. These results illustrate that the photoexcited electrons from the conduction band (CB) of ZnCr-LDH can inject into the valence band (VB) of Cu_2O , forming a Z-scheme heterojunction, by taking into consideration the band structure match between

Cu_2O and ZnCr-LDH.^{8,19,23} In such a Z-scheme photocatalyst, upon light irradiation, the photoexcited electrons from the CB of ZnCr-LDH can inject into the VB of Cu_2O through the bridge-type interface. The injected electrons neutralize the photo-generated holes of Cu_2O and inhibit its self-oxidation, giving rise to a largely enhanced photostability. The electrons from the CB of Cu_2O and the holes in the VB of ZnCr-LDH participate in the reduction and oxidation of water molecule to produce H_2 and O_2 , respectively (Fig. 4d). In addition, the transient XAS of the sample collected after photocatalytic reaction exhibits the same trend in the shift between light-on and light-off states, confirming the good stability of the photocatalyst (Fig. S8, ESI[†]).

The relationship between Cu–S bond modification and photoelectrochemical properties of the photocatalysts was investigated by transient current–potential, photoluminescence (PL) spectroscopy and electrochemical impedance spectroscopy (EIS) measurements. The photocurrent exhibits an obvious increase with the increment of r -parameter (Fig. S9, ESI[†]), which indicates an improved mobility of photoexcited charge carriers with the interfacial modification by the Cu–S bond. The PL intensity (Fig. S10, ESI[†]) of ZnCr-LDH (at 470 and 600 nm) shows a significant decline with the construction of the Cu–($\text{S}_2\text{O}_3^{2-}$)/LDH bridge structure, and the degree of reduction is positively correlated with the increase of r -parameter. This phenomenon implies that in the presence of the Cu–($\text{S}_2\text{O}_3^{2-}$)/LDH bridge structure, the excited electrons in ZnCr-LDH are inclined to migrate to Cu_2O instead of de-excitation to release fluorescence. The EIS test (Fig. S11, ESI[†]) shows that the charge-transfer resistance for the $\text{Cu}_2\text{O}@/\text{ZnCr-LDH}$ photocatalysts upon illumination is much lower than that without light irradiation. In addition, with the increase of r -parameter, the charge-transfer resistance decreases from 416 to 263 Ω (Table S3, ESI[†]), demonstrating that the charge transfer properties of the $\text{Cu}_2\text{O}@/\text{ZnCr-LDH}$ photocatalysts can be optimized through the modification of the Cu–S bond at the heterointerface.

The coincidence Doppler broadening (CDB) method in positron annihilation spectroscopy (PAS) is a powerful tool for nondestructive investigation of defects in materials.²⁴ However, to our knowledge, the CDB-PAS technique has not been used to reveal the charge transfer properties of a heterojunction photocatalyst. In PAS, the energy of the γ -photon captured by two identical high-purity germanium (Ge) detectors is described as $E\gamma$. Based on CDB treatment, two key parameters S and W are defined as the ratio of counts appearing in the central area of the 511 keV photo-peak ($|511 \text{ keV} - E\gamma| \leq 0.86 \text{ keV}$) and the wing region ($1.6 \text{ keV} \leq |E\gamma - 511 \text{ keV}| \leq 4 \text{ keV}$) to the total area of the photo-peak,^{25,26} to quantify the fraction of annihilated positrons with the low-momentum-electrons (valence electrons) and high-momentum-electrons (core electrons), respectively (Fig. 5a, eqn (2)).

$$\begin{cases} S = A/\text{sum} \\ W = (B1 + B2)/\text{sum} \end{cases} \quad (2)$$

In general, the S -parameter is a signature for the annihilation probability of positrons with valence electrons. In a photocatalyst with a heterostructure, if the S -parameter increases

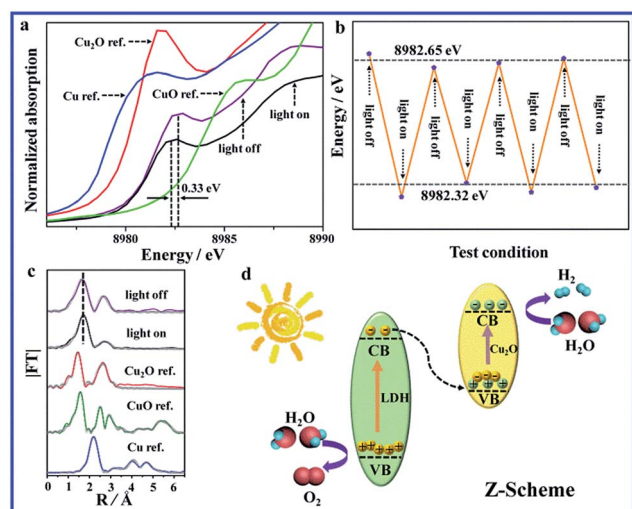


Fig. 4 Excited state XAS data of $\text{Cu}_2\text{O}@/\text{ZnCr-LDH-S}_4$ with and without light irradiation: (a) normalized XANES signals for the pre-edge region; (b) transient Cu K-edge XAS data and (c) Fourier transformed EXAFS signals from k^3 -weighted oscillations; (d) schematic illustration of the photoexcited carrier separation/transport in the $\text{Cu}_2\text{O}@/\text{ZnCr-LDH}$ photocatalyst.

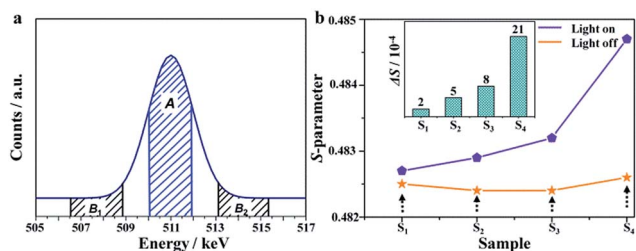


Fig. 5 (a) Schematic definition for S - and W -parameters in CDB-PAS measurements. (b) S -parameter for the different $\text{Cu}_2\text{O}@Zn\text{Cr-LDH}$ samples; the inset shows the difference in S -parameter (ΔS) between light on and off states.

under light irradiation, it means that the photoelectrons are prone to migrate from one semiconductor to another instead of recombination with holes, and *vice versa*. Based on the variation tendency of the S -parameter, a direct understanding of the migration ability of the photoexcited electron at the hetero-interface can be expected. The S -parameter for the $\text{Cu}_2\text{O}@Zn\text{Cr-LDH}$ samples was calculated using eqn (2) based on CDB-PAS. No obvious fluctuation of the S -parameter for S_1 – S_4 samples is observed without light irradiation (orange line in Fig. 5b). However, when the test was *in situ* performed under light irradiation, the S -parameter displays an obvious increase, indicating an enhancement of the annihilation probability of positrons with the low-momentum-electrons (valence electrons). Furthermore, the S -parameter exhibits an increase with the increment of r -parameter (purple line in Fig. 5b). In other words, as the r -parameter increases, the difference in S -parameter (ΔS) for the samples between dark and illuminated states increases (inset in Fig. 5b). The results above confirm that the transfer efficiency for the photo-induced carrier is improved with the successful construction and optimization of the $\text{Cu}-(\text{S}_2\text{O}_3^{2-})/\text{LDH}$ bridge structure at the heterointerface, which is responsible for the extremely high photocatalytic activity toward water splitting.

Conclusions

In summary, a $\text{Cu}_2\text{O}@Zn\text{Cr-LDH}$ photocatalyst with high activity toward visible light water splitting was obtained by elaborate modification and optimization at the heterointerface. By using the CDB-PAS technique, the transportation behavior of photoexcited electrons was traced for the first time, to reveal the relationship between the interfacial structure and the photocatalytic performance. Based on XAS, photocurrent, EIS and PL measurements, the photo-induced charge transfer behavior at the interface of a dual-semiconductor heterojunction has been understood in-depth and expounded. The excellent performance is attributed to the precise regulation over the $\text{Cu}-(\text{S}_2\text{O}_3^{2-})/\text{LDH}$ bond, which acts as a passing bridge to improve charge transfer and thus allows a high utilization of photo-induced carriers. It is expected that the insights in the present study will open up opportunities for the rational design and preparation of new photocatalysts with heterostructures.

Conflicts of interest

There are no conflicts to declare.

Acknowledgements

This work was supported by the 973 Program (Grant No. 2014CB932102), the National Natural Science Foundation of China (NSFC), the Fundamental Natural Science Funds for the Central Universities (buctylkxj01), the Young Elite Scientists Sponsorship Program by CAST, and the Beijing Nova program. We are thankful for the support of the Beijing Synchrotron Radiation Facility (BSRF) for the XAFS measurements. We also appreciate the kind help of Dr Alejandro Fernandez-Martinez from Université Grenoble Alpes, CNRS for the fitting of XAFS data.

Notes and references

- 1 T. Cao, P. Huang, K. Zhang, Z. Sun, K. Zhu, L. Yuan, K. Chen, N. Chen and Y. Li, *J. Mater. Chem. A*, 2018, **6**, 3435–3443.
- 2 M. Zhang, G. Wang, D. Zhao, C. Huang, H. Cao and M. Chen, *Chem. Sci.*, 2017, **8**, 7807–7814.
- 3 Y. Zhu, J. Ren, X. Yang, G. Chang, Y. Bu, G. Wei, W. Han and D. Yang, *J. Mater. Chem. A*, 2017, **5**, 9952–9959.
- 4 L. Liao, Q. Zhang, Z. Su, Z. Zhao, Y. Wang, Y. Li, X. Lu, D. Wei, G. Feng, Q. Yu, X. Cai, J. Zhao, Z. Ren, H. Fang, F. R. Hernandez, S. Baldelli and J. Bao, *Nat. Nanotechnol.*, 2014, **9**, 69–73.
- 5 J. Liu, Y. Liu, N. Liu, Y. Han, X. Zhang, H. Huang, Y. Lifshitz, S.-T. Lee, J. Zhong and Z. Kang, *Science*, 2015, **347**, 970–974.
- 6 C. Li, G. Chen, J. Sun, J. Rao, Z. Han, Y. Hu and Y. Zhou, *ACS Appl. Mater. Interfaces*, 2015, **7**, 25716–25724.
- 7 L. K. Putri, B.-J. Ng, E. W.-J. Ong, H. W. Lee, W. S. Chang and S.-P. Chai, *J. Mater. Chem. A*, 2018, **6**, 3181–3194.
- 8 A. Paracchino, V. Laporte, K. Sivula, M. Grätzel and E. Thimsen, *Nat. Mater.*, 2011, **10**, 456–461.
- 9 K. Iwashina, A. Iwase, Y. H. Ng, R. Amal and A. Kudo, *J. Am. Chem. Soc.*, 2015, **137**, 604–607.
- 10 A. Iwase, Y. H. Ng, Y. Ishiguro, A. Kudo and R. Amal, *J. Am. Chem. Soc.*, 2011, **133**, 11054–11057.
- 11 B. Liao, E. Najafi, H. Li, A. J. Minnich and A. H. Zewail, *Nat. Nanotechnol.*, 2017, **12**, 871–876.
- 12 Z. Zou, J. Ye, K. Sayama and H. Arakawa, *Nature*, 2001, **41**, 625–627.
- 13 J. Luo, J.-H. Im, M. T. Mayer, M. Schreier, M. K. Nazeeruddin, N.-G. Park, S. D. Tilley, H. Fan and M. Grätzel, *Science*, 2014, **345**, 1593–1596.
- 14 Y. Chen, S. Zhao, X. Wang, Q. Peng, R. Lin, Y. Wang, R. Shen, X. Cao, L. Zhang, G. Zhou, J. Li, A. Xia and Y. Li, *J. Am. Chem. Soc.*, 2016, **138**, 4286–4289.
- 15 K. Iqbal, A. Iqbal, A. M. Kirillov, C. Shan, W. Liu and Y. Tang, *J. Mater. Chem. A*, 2018, **6**, 4515–4524.
- 16 K. Hu, A. D. Blair, E. J. Piechota, P. A. Schauer, R. N. Sampaio, F. G. L. Parlane, G. J. Meyer and C. P. Berlinguette, *Nat. Chem.*, 2016, **8**, 853–859.
- 17 O. S. Wenger, *Chem. Soc. Rev.*, 2011, **40**, 3538–3550.

- 18 D. N. Beratan, J. N. Onuchic, J. R. Winkler and H. B. Gray, *Science*, 1992, **258**, 1740–1741.
- 19 C. Wang, B. Ma, S. Xu, D. Li, S. He, Y. Zhao, J. Han, M. Wei, D. G. Evans and X. Duan, *Nano Energy*, 2017, **32**, 463–469.
- 20 R. G. Pearson, *J. Am. Chem. Soc.*, 1963, **85**, 3533–3539.
- 21 K. Maeda, M. Higashi, D. Lu, R. Abe and K. Domen, *J. Am. Chem. Soc.*, 2010, **132**, 5858–5868.
- 22 S. Sun, W. Wang, D. Li, L. Zhang and D. Jiang, *ACS Catal.*, 2014, **4**, 3498–3503.
- 23 C. Silva, Y. Bouizi, V. Fornés and H. García, *J. Am. Chem. Soc.*, 2009, **131**, 13833–13839.
- 24 K. Verheyen, M. Jardin and A. Almazouzi, *J. Nucl. Mater.*, 2006, **351**, 209–215.
- 25 Y. Nagai, M. Hasegawa, Z. Tang, A. Hempel, K. Yubuta, T. Shimamura, Y. Kawazoe, A. Kawai and F. Kano, *Phys. Rev. B*, 2000, **61**, 6574–6578.
- 26 S. Dutta, S. Chattopadhyay, M. Sutradhar, A. Sarkar, M. Chakrabarti, D. Sanyal and D. Jana, *J. Phys.: Condens. Matter*, 2007, **19**, 1–11.